

Multiple-order moments of the transient electromagnetic response of a one-dimensional earth with finite conductance – the Gaussian variation applied to a field example

Richard S. Smith¹ and Terry J. Lee²

¹Harquail School of Earth Sciences, Laurentian University, 935 Ramsey Lake Rd, Sudbury, Ontario, P3E 2C6, Canada

²Independent Consultant, GPO Box 1984, Canberra, ACT, 2601, Australia

Right running head: Field example of Gaussian conductivity variation

Table of contents (TOC) short summary:

Using higher-order moments of the electromagnetic response, it is possible to invert data to find a conductivity model that varies smoothly with depth described by a Gaussian function. The Gaussian can approximate thin sheets, thick sheets and more general variations. In the case of our field area, we obtained results more consistent with geological control using the general variation.

This is a preprint of the paper published as

Richard S. Smith and Terry J. Lee, 2021, Multiple-order moments of the transient electromagnetic response of a one-dimensional earth with finite conductance – the Gaussian variation applied to a field example, *Exploration Geophysics*, DOI: 10.1080/08123985.2021.1925105

Abstract.

Formulae for the moments of the magnetic field response can be derived for simple models which have conductivities that vary suddenly as a function of depth (thin and thick sheets) or not at all (half space). In a companion paper we have derived expressions for the moments of a conductivity-depth profile that varies smoothly, taking the form of a Gaussian function. In this paper we apply the Gaussian model to data from Russell South, an area in the Athabasca Basin of Canada. The low signal-to-noise ratio in this area means that estimating the overburden thickness is a challenging problem, so this dataset is a good candidate for demonstrating the applicability of our approach. The estimated thicknesses can be compared with drill information, also somewhat problematic as a reliable source of information. If we constrain the Gaussian model to be similar to a thin sheet or a thick sheet at surface, we get estimates of the overburden thickness which are much greater than what is inferred from drill information. However, if the overburden is allowed to vary gradually and the depth and value of the maximum conductivity can vary, then we find that the depth of the most conductive part of the overburden is realistic as it is generally above the base of overburden as determined from drilling. Features of geological interest that are not apparent on the original data can be identified on the derived images.

Keywords: Airborne electromagnetics, Canada, Case histories, Conductivity, Interpretation, Inversion, Mineral exploration, Multicomponent, Uranium exploration, Athabasca basin

Introduction

The moments of the electromagnetic response are quantities that can be calculated from the measured transient electromagnetic response (Smith and Lee 2002a). The n th-order moment of the i th component of the magnetic-field step response (Lee and Smith 2021) is obtained by multiplying the decay, $B_i(t)$ by t^n and integrating this product from the step ($t = 0$) to the latest possible delay time ($t = \infty$), viz., $M_i^n = \int_0^\infty B_i(t) t^n dt$. In this paper, we only use the zeroth and first moments, $n = 0$ and 1 . The advantage of the moments is that for some simple models, the moments can be calculated very quickly and easily compared with the moments calculated from a measured electromagnetic (EM) response. Formulae for moments have been derived for a number of geoelectric models: spheres in a uniform field (Smith and Lee 2001), wire-loop circuits, spheres in a dipolar field (Smith and Lee 2002a; 2003), thin sheets, thick sheets and half spaces (Smith and Lee 2002b; Lee et al. 2003), and a sphere below an overburden (Desmarais 2018a; 2018b). These models have been used to estimate the conductance and conductivity (Smith 2000; Smith et al. 2005) and to model or invert EM data (Hyde 2002; Smith et al. 2003; Smith and Salem 2007; Schaa and Fullagar 2010, 2012; Fullagar and Schaa 2014; Fullagar et al. 2015). Moments have also been used to map airborne EM data (Bournas et al. 2018) and interpret electromagnetic data for detecting unexploded ordnance (Snyder et al. 2010; Hall 2014).

A disadvantage of moments is that the theoretical moments assume ideal step or impulse waveforms and an infinite off-time, assumptions which are rarely true in practice. However, the workers cited above have used moments estimated from non-ideal realizable waveforms using windowed data and they have obtained reasonable results.

In general, the geoelectric models used have conductivities which are either constant, or vary suddenly as a function of depth. For example, the half-space model has a conductivity which is finite and constant below the earth's surface and zero above; the thin sheet model increases its conductivity suddenly, then decreases again at an infinitesimally greater depth in such a manner that the conductivity-thickness product (conductance) is finite; the thick sheet has a constant conductivity from surface to the base of the

sheet and then below that is either zero (Smith and Lee 2002b) or finite (Bagley 2019). Recognizing that these are special and idealized situations and that the conductivity can in reality vary more smoothly as a function of depth, Lee and Smith (2021) have derived formula for the moments of an earth which has a conductivity that varies as a Gaussian function, in which the conductivity is a maximum at a specific depth, but drops off exponentially above and below that depth. Other workers (Lee and Ignetik 1994) have looked at EM solutions of earths with exponential variations of conductivity with depth.

The most common one-dimensional geoelectric model used in electromagnetic methods is a multi-layered earth (Morrison et al. 1969; Farquharson et al. 2003). However, many different layered models can frequently explain the data, so some type of regularization (e.g. smoothing) is usually required and the final model will depend on the amount of regularization applied. Simplifying the model to a few layers can reduce the ambiguity (e.g. Smith et al. 2004), but this can also be problematic as the number of layers used in the inversion might have to be changed along a profile line and deciding when to make this change is non-trivial. It is possible to use sophisticated and computationally expensive tools such as transdimensional Markov chain Monte Carlo methods to estimate the appropriate number of layers (Brodie and Richardson 2013). An advantage of the Gaussian model that we defined below is that it is a simple model, described by just three parameters: a maximum conductivity value, the depth that the maximum occurs and the rate that the conductivity falls off above and below the maximum value. These three parameters can be adjusted, to explain the measured data. The Gaussian model can be used to approximate one-, two- and three-layer models, and the transition between these models is automatically handled by the inversion algorithm when adjusting the three parameters.

In this contribution we apply the Gaussian model to data from an area, Russell South, in the Athabasca Basin, located in Saskatchewan, Canada. When the Gaussian model is constrained to be like a thin sheet, we can derive quantities related to the conductance and depth of the sheet; when it is constrained to be like a thick sheet, we can estimate quantities related to the conductivity and thickness. In the case when no constraints are applied, the maximum conductivity, depth of the maximum conductivity and half width

of the Gaussian function can be estimated. Images of these quantities can be used to interpret geological features. In our field example, there is one linear geological feature that is not evident on the original on-time data but is evident on some of our derived images.

Field data

Airborne transient electromagnetic data has been collected in an area of the Athabasca Basin using the GEOTEM electromagnetic system (Annan and Lockwood 1991). The system was configured to operate at a 90 Hz base frequency with a 2.2 millisecond (ms) pulse and a dipole moment of 672000 Am². The primary fields as measured using the x -, y - and z -component receivers are shown on Figure 1. The transmitter was nominally 120 m above the ground and the multicomponent receiver was towed 130 m behind and 50 m below the transmitter mounted on the aircraft.

Russell South Area

The data was collected for Roughrider Uranium Corp (Fugro 2005a), primarily to explore for deep graphitic sediments in the basement below the Athabasca sediments (Fugro 2005b), as these graphites are often associated with uranium deposits. These conductors have large amplitude and slow time decays, so a 2 ms pulse and wide windows at late time are appropriate. The time that the GEOTEM transmitter pulse ends is not tightly controlled so the window positions will vary with respect to the end of the pulse during the survey. As well, the window widths are not particularly narrow when they are close to the pulse. This variation in window position and the wide window widths means that the GEOTEM system is not optimally configured for resolving the rapid decays associated with near-surface conductivity structures. A more optimal system for overburden mapping might be a system with a well-controlled switch off and narrow windows close to the end of the transmitter pulse, such as the TEMPEST system (Lane et al. 2000) or the MULTIPULSE system (Chen et al. 2015). Even though the survey system is not optimal it can still be used to show the benefits of the Gaussian model and how the higher-order moments for the x - and z -components can be used to extract information from the EM data.

The survey area is generally resistive, with most responses having decayed by window 8, which is about 0.413 ms after the middle of the ramp at the end of the switch off of the pulse (Fugro 2005b). The slow decay associated with graphitic conductors common in the Athabasca Basin are not evident in the area. An example profile (Figure 2) shows the on-time z-component response (black line), the on-time x-component response (grey line) and the off time z-component responses (dashed lines). These B-field responses are calculated from the dB/dt responses using the procedure of Smith and Annan (2001). The anomalous response associated with a power line is evident to the left of the profile near 471000 E (marked with a number sign, #), a weakly conductive feature typical for this survey area is evident near 4775000 E (marked with an asterisk, *). This weakly conductive feature is most likely conductive glacial or fluvial overburden (Fugro 2005b). The right half of the profile has an off-time response that shows no decay or an extremely small decay, so this area has an overburden that is either more resistive or thinner.

The weakly conductive zones are relatively broad, a few km in width. However, the data also show oscillatory features with a wavelength of about 200 to 300 m. In many cases a decrease in the z component on-time response shows an increase in the corresponding x-component response and vice versa, for example between 481000 E and 482000 E. This is interpreted as being due to changes in the coil orientation, most likely due to the bird swinging (Davis et al. 2006; 2009). We found that applying a filter with a half width of 45 points (500 m) suppressed these oscillations and retained the signal associated with the weakly conductive zones.

Figure 3 shows two typical transients, the one at the position marked with an asterisk is the weakly conductive feature (solid line) and it has decayed to the noise level (1000 fT) by about 0.6 ms. The other (dashed line) is from the more resistive area at 480000 E and shows a response that is effectively zero at all but zero time or on-time window 5. Annan et al. (1996) have shown that the on-time data are sensitive to the conductivity even in resistive areas where the off-time response is small. Various other methods have been developed to also use this on-time data (Smith 2000; Bagley 2019). Limited information can be extracted from this on-time data, as there are only two pieces of information, the x and z-component

windows, so examples of the parameters that are typically estimated are the thin-sheet conductance or the half-space conductivity and possibly the depth to these structures. The standard approach for interpreting time-domain electromagnetic data is to process or fit the off-time data, but this is only useful where the off-time response is large. The moments combine both on-time data and off-time data, so should be able to extract geological information from the on-time data and if there is an observable off-time response, we should be able to use this additional information as well.

The first moment ($n = 0$ in the moment integral) is just the area under the decay curve. For the dashed-line case in Figure 3, there is a strong contribution from the on-time data close to $t = 0$. While for the solid-line case, there is a larger contribution from the off time data. As the moment order, n , increases, the moment integrand is weighted by t^n , so greater emphasis is placed on the off-time data,, as t is large in the off time. However, any late-time noise will also be amplified in the higher-order moments. In this paper, we calculate the moments using the method described at the beginning of the next section.

The topography of the survey area and the airborne electromagnetic traverse lines can be seen on the digital terrain model (DTM) image shown on Figure 4a, which is derived from the height of the aircraft (determined via real-time differential corrected GPS data) and the radar altimeter. The height varies by a maximum of about 45 m and is largely attributed to glacial features such as drumlins or eskers.

The on-time data shows some strong responses and distinct features. Figure 4b is the map of the x -component window 5 image of the area and Figure 4c is the corresponding z -component image. Window 5 is centred on the transmitter switch off ramp and hence is an on-time window. These two maps (Figures 4b and 4c) are quite similar, with the z -component having larger amplitude and hence a larger signal-to-noise ratio.

Some low-lying areas A, B and C are evident as purple or dark blue features on the DTM (Figure 4a) corresponding to large (conductive) responses with comparable shapes on the x -component on-time image (Figure 4b). These are likely weakly conductive sediments associated with current or former lakes or swamps in these areas. However, not all low-lying areas have a conductive response. Areas which are

topographic highs on the DTM are often resistive, although the shapes of the topographic highs do not correspond closely to the shapes of the resistive features. For example, there are some north-northeast and north trending topographic highs two and four km east of A, but the resistive area within which they lie is much larger and has no specific trend. Location D is also a topographic high trending north-northeast, but the purple resistive feature does not show a corresponding trend. Further, there is a north-northeast trending conducting feature less than a km to the south east of D. Two discontinuous conductive trends running north-northwest are evident on the conductivity image (shown with white dash-dot lines on Figure 4b). These are marked with the label E at their southeast end. There is no corresponding feature on the DTM, so these appear unrelated to topography. Hence they could be conductive features within the overburden. Interestingly, these linear features crosscut topographic highs, but the most conductive parts do not correspond with just topographic highs or lows. Joining discontinuous features is an interpretive process and alternate interpretations are possible; for example, the white arrow at the southern end of Figure 4b shows a trend direction running parallel to the topographic trend and there are three discontinuous conductive features along this trend, one on each of the dash-dot lines and the third feature southeast of D.

Figure 4c, the z-component response, shows very similar features to the x component, except the response amplitudes on the z component are greater and the features are broader and show less asymmetry due to diminished flight-line direction artifacts (Smith and Chouteau 2006).

Interpretation methodology

At each location where the transient airborne electromagnetic response is measured, the multiple-order moments were calculated from the field data using the approximate method described by Smith and Lee (2002a) which integrates the B-field data and assumes that the half-sine current pulse is an impulse, with the centre of the pulse being zero time. This assumption for zero time gave good results in the area tested by Smith and Lee (2002), the conductive clay belt north of Timmins. However, we found that in the highly resistive Athabasca Basin, better (non-negative) results were obtained if we assumed that the impulse

was the spike in voltage associated with the pulse switching off. In this case, we put zero time at the start of the last on-time window 5 (2.17 ms), which is centred on the switch off and has the largest signal (Annan et al. 1996). We spent some time experimenting with different zero-time positions and found that other positions did not give improved results with less negative moments or less erratic artifacts in the images. An alternate method, only applicable to estimating the zeroth-order moment, is to use the window at the start of the on-time (Annan et al. 1996). This alternate method was used by Bagley (2019).

The conductivity variation as a function of depth, z , is assumed to be described by a Gaussian function, which takes the form

$$\sigma(z) = A_0 e^{-b(z-c)^2}, \quad (1)$$

where, $\sigma(z)$ is the conductivity, A_0 is the maximum conductivity at a depth, $z = c$, and b controls the thickness of the layer or the narrowness of the peak. A useful way to characterize this narrowness is to calculate the half width of the conductivity function, $hw = \sqrt{\ln 2/b}$, which is the distance between the locations where $\sigma(z) = A_0/2$, i.e., $\sigma(c - hw/2)$ and $\sigma(c + hw/2)$. The Gaussian model reduces to the thin-sheet, thick-sheet and half-space models in limiting cases (Lee and Smith 2021). For example, if the half width, hw , is infinitesimally small, then the Gaussian is like a thin sheet, with the conductance being the area under the Gaussian curve (approximately A_0 times hw), see the black case in Figure 5. In the limit of hw extremely large, the conductivity is essentially constant as a function of depth, which is a half-space model (blue case in Figure 5). If the depth of maximum conductivity, c , is set to zero then we have an asymmetric half-Gaussian function; and if hw is not extremely large or small, then the maximum is at the surface and the model is somewhat like a thick sheet with the base of the sheet being at hw (red case in Figure 5). However, the conductivity does not change suddenly at the base of the sheet, it drops off gradually; the deeper the base of the thick sheet, the more gradual the change. The Gaussian model can also approximate cases when the conductivity increases gradually with depth (green case in Figure 5).

Formulae for deriving the moments of an earth model with a Gaussian depth dependence are presented by Lee and Smith (2021; see Appendix below for corrigenda). The moments are not linearly related to the parameters that describe the conductivity/depth variation, so a non-linear inversion method is required to determine the values of the three Gaussian parameters that minimize the residual between the measured and calculated moments. The method we used is the Levenberg-Marquardt inversion method as implemented in the `leastsq` routine in the `scipy.optimize` library

(<https://docs.scipy.org/doc/scipy/reference/generated/scipy.optimize.leastsq.html>). This routine is a wrapper for the MINPACK's `lmdif` and `lmder` algorithms (netlib.org). In order to get realistic positive values, we inverted for the log of the parameters (A_0 , c and b).

In order to show the different ways that our model can be applied we have inverted the survey data for three cases, 1) when the half width of the conductive layer is constrained to be a specified value ($hw = 5$ m); 2) when the most conductive part is constrained to be at surface ($c = 0$); and 3) when there are no constraints on any parameter.

Case 1: $hw = 5$ m, thin-sheet analogue

In the first case, we set the half width to be 5.0 m, so the geoelectric structure is essentially a thin sheet, with the two unknowns being the maximum conductivity, A_0 , and the depth of maximum conductivity, c . These unknowns can be determined with two knowns, the zeroth-order step-response moments for the x - and z -component measured response, calculated in the manner described above. The initial guess for the maximum conductivity was the conductance divided by the width, where the conductance is estimated from using the thin-sheet method of Bagley (2019) and the depth was the depth of a thin sheet estimated using the same method. We found that changing the initial guess gave similar results, so the method is largely independent of the initial guess. Figure 6a shows the maximum conductivity, A_0 ; Figure 6b is the half width, hw , which is constant and equal to 5 m; and Figure 6c is the depth of maximum conductivity, c . Locations A and C appear as conductive, however, a large square area with A and C as the approximate vertices is also mapped as relatively conductive; this square area was not apparent on either of the on-

time images on Figure 4. Location B however, is relatively resistive, with only small features corresponding poorly to the arcuate feature in the DTM and the on-time responses. The two dashed lines do not have coherent features associated with them: what appeared as conductive on the on-time images is more resistive on the maximum conductivity image. The feature with the large on-time response southeast of D is also resistive. The depth of maximum conductivity (Figure 6c) shows a shallow linear feature F, indicated by the black arrow in the northwest of the area, which is not evident on any of the previous images of the data, either in this paper or in Fugro (2005b) or Bagley (2019). Feature F occurs in an area that is interpreted to be moderately conductive from the on-time data (Figure 4b and 4c), so it could be a noise artifact, but this is less likely than if it were in a more resistive part of the survey area. This feature is close to a power line but is unlikely to be due to the power line as it trends at a different angle.

The conductive area (with A and C as approximate vertices), appears primarily green on Figure 6c, so the depths to the maximum conductivity in this area is between 80 and 130 m. The more conductive parts at A, B and C are shallower. As well, the conductive zones along E and southeast of D also appear as shallow. We interpret that the locations with the larger on-time responses are estimated by the inversion to be more shallow, with the maximum conductivity being adjusted to give a good fit. We suspect that in cases when both the x and z zero-order moments are large, the depth is well resolved and shallow, but otherwise the depth is not well resolved, so the inversion algorithm pushes the depth of maximum conductivity deeper.

Case 2: $c = 0$ m, thick-sheet analogue

In the second case, we set the depth of the maximum conductivity to be $c = 0$, so the geoelectric structure is essentially a thin or thick sheet at surface (half-Gaussian), with the two unknowns being the maximum conductivity, A_0 , and the half width. These unknowns can be determined with two knowns, the zeroth-order step-response moments for the x and z components, as for case 1. The initial guess for the maximum conductivity was the conductivity derived from the half-space model (Smith and Lee 2002b),

and the guess for the half width was 30 m. Figure 7a shows the maximum conductivity at surface; Figure 7b is the half width and 7c shows the depth of maximum conductivity, constrained to be at surface, $c = 0$. The maximum conductivity map is similar to the two on-time responses, with the conductive features being evident at A, B, and C, southeast of D and at the same locations on E. There is additionally a conductive linear feature evident at the same location as F. The fact that it is conductive suggests that the response might be stronger so the feature could be real and not a consequence of noise.

There are some unrealistically conductive features at the edges of the maps and we are not sure of the explanation for this. We speculate that they might be a consequence of the filtering done to the data to remove sensor-coil orientation oscillations. If this filtering is done when the data for the whole flight is included in the database, rather than after the data has been broken into lines that are limited to the survey area, then these noise artifacts might not be so apparent. The half-width image shows the shallowest features at locations where the maximum conductivity is largest. Again, where the area is not conductive, the small responses do not seem to constrain the half width, so the algorithm pushes the results deep, in some cases very deep (where there are black spots).

Case 3: unconstrained case

In this third case, there are no constraints, so we solve for all three unknowns A_0 , b and c . In this case, the Gaussian model can represent a thin or a (smoothly varying) thick sheet at any depth, a halfspace or an earth which has a conductivity that increases or decreases gradually with depth. The three unknowns can be determined with three knowns, the zeroth-order step-response moments for the x and z components and the first-order step response moment for the z component. We elected not to include the first-order x component moment as this was smaller in amplitude than the z component and more strongly impacted by noise. The initial guess was based on the thin-sheet solution of Bagley (2019), with the maximum conductivity A_0 being the conductance divided by the depth of the thin sheet, the depth of maximum conductivity, c , is the depth of the thin sheet and the half width was initialized to be half the thin-sheet depth. Figure 8a shows the maximum conductivity, with the area between A and C being primarily green,

with values around 3 mS/m. The black/red features in this zone are close to the power line, so are erratic results where the data are adversely impacted by large-amplitude power-line noise. Other black/red features appear erratically elsewhere in the image are interpreted to be due to other sources of low-amplitude noise in the areas where the signal strengths are weak. The features close to B, along E and southeast of B have conductivities around 0.8 mS/m, which is more conductive than the surrounding areas, but still very weakly conductive. The half-width image (Figure 8b) shows the layers as purple (narrow) at A and C, but at B, southeast of D and along E, the colours are generally green, indicating a more gradual conductivity variation with depth. The northern linear feature E is more coherent in this half-width image than in previous images as it can be seen as a linear zone of green and blue colours between red areas. The depth to maximum conductivity image (Figure 8c) shows shallow depths at B, C and northwest of A, but south of A and northeast of C, the depth of maximum conductivity is deeper, close to 100 m or more. The depths along E are variable, being of the order of 20 m in some cases, but closer to 100 m in other cases. This variability might be a consequence of the topographic variation. Feature F is most evident as a shallow feature on Figure 8c and has a moderate conductivity (Figure 8a).

There is some correlation/anti-correlation evident on the three panels of Figure 8. For example, the hot and cold colours on Figure 8a are generally hot and cold on Figure 8c, but are the opposite cold and hot on Figure 8b. The correlation/anti-correlation might be due to some inherent non-uniqueness in the problem resulting in cross-talk. However, there are other features that indicate this is not always the case. For example, feature F, evident as a cold (blue-purple) linear trend on Figure 8c is not cold on Figure 8a. Also, the area above D on Figure 8a is cold, but it is hot or warm on Figure 8c. However, this area should be interpreted with caution, as this is an area with very small signal, so the signal-to-noise ratio will be low and the moments might be less reliable. EM data should always be interpreted with caution in noisy areas and checked with independent data if possible.

Comparison of results from different cases

The numerical results we obtain for the Russell South area give different results depending on whether we constrain certain parameters or not. Broadly speaking, the two constrained cases give results that either look the same as the on-time data (highs and lows on one image corresponding to highs and lows, respectively on the other) or have the opposite appearance, with highs corresponding to lows and vice-versa. The unconstrained case seems to show more variability, presenting information present in the two constrained cases, plus additional information which might be reflecting geological variations. As there are three independent images in case 3, rather than two images in the others cases, we argue that there is more information available. Ternary images or ratio images of the Gaussian parameters might reveal subtle anomalies that could be of interest.

In the resistive areas, where both the on- and off-time off-time responses are relatively small, the parameters are not well resolved, so the half width, hw , or depth of maximum conductivity, c , tends to be erratic or unrealistically large. We feel this is because the model parameters are not constrained by the data and are set to large values by the inversion algorithm. In the third case, when the higher-order moment is used this noise is amplified. The areas with larger off-time responses are less noisy, with the images being more coherent.

Feature F is not seen on the original on-time data. Nor is it seen on the images generated by Bagley (2019), derived from on-time data only. This suggests that the feature might be a consequence of the subtle variations in the relative size of the x and z on-time responses or the contributions that off-time data make to the moments. The feature could also be a consequence of noise or human infrastructure, so it should be checked using an independent source of information. Nevertheless, the fact that this feature is not seen on the other images derived from the data suggests that additional information can be extracted using our method. For the thin-sheet model (case 1), feature F appears on the depth of maximum conductivity image; whereas for the thick-sheet model, the feature is visible on the maximum conductivity and half-width image. Hence it is not clear if the feature is related to the geoelectric or geometric parameters of the ground. However, on the unconstrained image, it is only evident on the

depth of maximum conductivity image, suggesting the feature is related to the geometry of the conductivity feature, not the conductivity.

In the thin-sheet cases, the areas with small on-time responses, have a low maximum conductivity and a shallow depth to maximum conductivity, which is plausible. The areas with large on-time responses have a large maximum conductivity, which is also plausible, but the depth to the maximum conductivity is large, in many cases greater than 100 m, which is less plausible. In the thick-sheet case the areas with small on-time responses also have a low maximum conductivity and a thin layer, which is again plausible. However, the thickness of the conductive layer in the conductive area is greater than 400 m, which is implausible. The unconstrained case has the maximum conductivity large in areas of large on-time responses and generally small, but more variable in other areas. The half width and the depth of maximum conductivity of the layers in the conductive areas are smaller and shallower respectively, being more plausible. In the resistive areas, the half widths and thicknesses are more erratic, but this will not have a significant impact on the response, as the layer is either resistive or deep.

In order to check the estimates of overburden thickness against ground truth, we need an independent source of information. The Saskatchewan Geological Survey has a drill-hole database available. One of the pieces of information in the database is the casing depth. In a simple scenario, drill holes will typically be cased through any unconsolidated material such as overburden and the casing will not be used in consolidated rock. Hence, in this scenario, the casing depth should be a good estimate of the thickness of overburden and could be compared to the depth estimated from the inversion results. However, such a comparison with the casing depth will be imperfect for a number of reasons:

- 1) there is sometimes a gradual transition from unconsolidated overburden to consolidated bedrock and the casing will be used until the driller is certain that consolidated bedrock has been reached. Some drillers will be more conservative than others and make the casing deeper.
- 2) There is a scale issue in that the drill hole is only sampling a very small area a few tens of square centimetres, where the airborne EM system is sensitive to thousands of square metres.

- 3) The drill locations are not exactly coincident with the location of the flight lines, some drill collars might be midway between lines and the overburden thickness can vary significantly over such distances.
- 4) The casing depth is the depth of unconsolidated overburden, however, the airborne EM method is sensitive to the conductive material in the overburden. If the conductive material is higher up, the casing depth will be deeper than the estimate from the airborne EM data.
- 5) Drilling through overburden is problematic, so drill locations will be selected away from eskers etc., and in areas where the overburden is expected to be thin. This will bias the sampling of the casing depth to be thinner than it might be if the drill locations were selected more representatively.
- 6) Some drill locations might be reported using an incorrect reference ellipsoid (NAD27), so these locations will be incorrect.
- 7) The top of the sandstone bedrock below the overburden may be weathered and have a similar conductivity to the overburden, meaning that electromagnetic methods cannot identify the overburden/bedrock boundary and hence the thickness of overburden.

Also, the inversion results are not expected to be flawless either. When the signal is small, results can be erratic, so we have only compared the results where the conductivity on Figure 7a is greater than 1 mS/m, as this ensures larger signals. Even in these conductive areas inversions can still return erratic results, so unrealistically large depths (e.g. greater than 500 m on Figure 7b) have been removed. Also, the drill collars are not on the flight lines, so we have searched for all EM-derived depth estimates within 170 m of the drill collar. The most reliable depth estimate is the minimum value, so we have taken the minimum of all the values within the 170 m search radius.

In the following analysis we look for a relation between the casing depth and the EM-derived depth. In our ideal scenario, the drill would be in an appropriate location and the casing will indicate the depth of unconsolidated overburden and the unconsolidated overburden will be uniform and more conductive than the bedrock, so the EM estimate should be equal to the casing depth. In that case, if we were to plot

the EM-derived thickness estimated against the casing depth, we should get a straight line, with a zero intercept and a slope of unity.

In case 1, the estimated depth from the EM data is the bottom of the layer, $c + hw$, which has been plotted against the casing depth on Figure 9a. There is not a strong correlation between the casing depth and the estimated depth. The most important parameter is how large these estimated depths are relative to what they should be and of secondary importance is how much scatter there is. The relative magnitude of the estimated depth can be quantified by fitting a straight line with a zero intercept and a variable slope to the data. If the estimated depths are too large, the slope will be larger than unity; while small depth estimates will result in slopes less than unity. The fitted straight line (solid black line on Figure 9a) has a slope of 1.65, which says that on average the estimated depth of the conductive feature is 1.65 times greater than the casing depth, which is unrealistic, as the casing ends in well consolidated (resistive) Athabasca sediments. The scatter of the results is quantified by the fitting parameters, in this case a large scatter is indicated by a large residual sum of squares and small Pearson's r and R-square parameters (see Table 1).

For case 2, the maximum conductivity is fixed to be at surface ($c = 0$) and the depth to the bottom of the layer is the half-width, hw . Figure 9b shows the cross-plot and the straight line is the linear fit with zero intercept. In this case, the slope is 3.3, which implies that the estimates are far too deep. The fit parameters also indicate a poor fit. This suggests that constraining the maximum conductivity to be at surface is definitely not appropriate in this area.

In the unconstrained case (3), we invert for hw and c , so the conductive overburden depth could be $c + hw$ or c . The cross plot of $c + hw$ against the casing depth is shown on Figure 9c. The slope is large 2.62, as is the scatter, so $c + hw$ is not a good depth estimate of the thickness for this case. If c is used as the depth estimate, we obtain the cross-plot on Figure 9d. This case has a slope of 0.76, which is reasonable, when you consider that the overburden can be comprised of resistive and conductive layers of material. These conductive layers could be at the base of the overburden, at surface, or somewhere in between, so the casing depth is the upper limit of the depth of the conductive feature in the overburden. Having the

conductive layer with a maximum on average at 76% of the depth of the casing is therefore reasonable. This is the only reasonable case, so we conclude that the full unconstrained Gaussian model is the most appropriate model and that the depth to maximum conductivity provides the best estimate of the depth (Figure 9d).

The residual sum of squares for Figure 9d is small (Table 1), however, the depth values are all small, so this is expected. The large scatter apparent in all cross plots reflects the noise in the EM data and the imperfection of using casing depth as a proxy for overburden thickness. Hence not too much attention should be paid to the fitting parameters. In cases (1) and (2) we have two parameters that can be varied in the inversion. In case (3), there are three parameters (more degrees of freedom), so the inversion program has more parameters it can adjust to improve the fit and this is another explanation for the reduction in the Pearson's r parameter.

Discussion

The above results are applicable for the Russell South area; for another area, the model that should be used will depend on the parameter of interest and the character of the overburden. In some survey areas, simple thin or thick sheet models may be appropriate if the overburden varies as a thin or thick sheet. However, over large areas where the character of the overburden may change, a more flexible model such as our Gaussian model may be required. If there is some geological control, then different cases of this more flexible model can be tested to see which case is most appropriate and gives the most reasonable results.

The Russell South area is highly resistive and used an EM system with limited high-frequency information. Better results might be obtained with more optimal systems designed for collecting high-frequency information with narrower windows that are closer to the end of the pulse and a transmitter pulse that switches off at a well-controlled time.

There are a number of improvements to this method that could be applied when further work is undertaken on this topic. Firstly, the parametric inversion allows the uncertainties or confidence limits for the model parameters to be estimated (Jupp and Vozoff 1975; Press et al. 1992). Doing this would enable identification of the more and less reliable solutions.

The question of non-uniqueness needs to be investigated when inverting multiple-order moments. One potential source of non-uniqueness is the conductivity/thickness trade off. In such cases, the posterior covariance matrix or correlation matrix will show that the conductance, which is proportional to $A_0 hw$ or A_0/\sqrt{b} is reliably resolved by the inversion although A_0 and b might not be. In these cases, it might be useful to make maps of the conductance. Comprehensive explorations of parameter space using Markov chain Monte Carlo techniques (e.g. using PyMC3 described at <https://docs.pymc.io/>) could also identify trade-offs or non-uniquenesses between parameters.

Finally, in our inversion we have selected the minimum number of data required to resolve the parameters of interest. That is, when wanting to determine two parameters, we used two moments and when three parameters are sought we used three moments, with preference for the moments with the higher signal-to-noise ratios. Using all available moments (and possibly fractional-order moments) could stabilize the inversion and improve the uncertainties in the estimates.

Conclusions

The Gaussian conductivity distribution represents a model that allows us to estimate the moments when the conductivity changes gradually as a function of depth, something that will occur in nature in many circumstances, but cannot be modelled analytically with 1) the thin-sheet, 2) thick sheet and 3) half-space models. The Gaussian model can approximate the above three limiting cases when the model parameters are constrained. Hence the Gaussian model provides different options for calculating the moments of a variety of real-world situations.

Measured data can be explained using an inversion algorithm to adjust the three parameters of the Gaussian model. One of the advantages of the Gaussian model is that with just three parameters, it provides a simple model capable of approximating a wide variety of different types of geoelectric variations: gradual changes in conductivity with depth (hw large), rapid changes in conductivity with depth (hw small), conductive material at surface ($c = 0$), intermediate depth, and conductivity increasing at depth (c large). Furthermore, the Gaussian model can approximate one-, two-, or some three-layer models automatically, by adjusting the values of the parameters.

In a field example from Russell South, we used the Gaussian model to estimate the parameters of the overburden. When these estimated values were imaged, features became evident that were not obvious in the original data. We experimented with constraining some parameters of the model, but we found that using no constraints, and solving for the maximum conductivity, A_0 , depth of maximum conductivity, c , and half width, hw , would give reasonable depth estimates if we took the depth of maximum conductivity as the depth to a conductive feature within the overburden package. In other survey areas, experimentation would be required to determine which model is appropriate, or whether a specific constraint is appropriate.

Acknowledgements

Richard Smith is grateful to an NSERC Discovery Grant for supporting this work. We are grateful to the assistance of Thomas Bagley in helping get us the field data. The Fugro reports can be found on the Saskatchewan Mineral Assessment Database by searching for digital submissions from 2005 lodged by Roughrider Uranium under assessment file number 74H06-0127. They can also be obtained from the corresponding author.

We are grateful to the comments of anonymous reviewers who suggested further improvements that could be made to the implementation. These are outlined in the Discussion section above.

Appendix – Corrigenda to Lee and Smith (2021)

The mathematical theory in the companion paper (Lee and Smith 2021) contains a number of errors we have identified since its publication.

1) The line following equation (15) should start: “where $s = i\omega$.”

2) Equation (16) of the companion paper should read

$$H_j(t) = \frac{1}{2} a I_0 \int_0^{\infty} J_1(\lambda a) J_l(\lambda r) \lambda e^{-\lambda|h+z|} R_E(\lambda) \sum_{i=1}^{\infty} (e^{-\lambda_i t}) / \lambda_i d\lambda. \quad (16)$$

3) The paragraph following the sentence containing equation (19) which reads:

“The time-independent $1/\lambda_i$ term in the sum in Equation (16) is ignored as off-time EM methods typically only record the transient response”

should be deleted.

References

Annan, A.P., and R. Lockwood. 1991. An application of airborne GEOTEM in Australian conditions.

Exploration Geophysics **22**: 5-12. <https://doi.org/10.1071/EG991005>.

Annan, A.P., R.S. Smith, J. Lemieux, M.D. O'Connell, and R.N. Pedersen. 1996. Resistive-limit time-domain AEM apparent conductivity. *Geophysics* **61**: 93-99. <https://doi.org/10.1190/1.1443960>

Bagley, T. 2019. *Estimating overburden thickness in resistive areas from on-time airborne EM data. MSc thesis, Laurentian University.* <https://zone.biblio.laurentian.ca/handle/10219/3384> (Accessed 28 May 2020).

Bournas, N., A. Prikhodko, K. Kwan, J. Legault, V. Polianichko, and S. Treshchev. 2018. A new approach for kimberlite exploration using helicopter-borne TDEM data. *SEG Technical Program Expanded Abstracts 2018*: 1853-1857. doi: 10.1190/segam2018-2996206.1

Brodie, R.C., and M. Richardson. 2013. AEM system target resolvability analysis using a Monte Carlo inversion algorithm. *ASEG Extended Abstracts 1-4*: DOI: 10.1071/ASEG2013ab227

Chen, T., G. Hodges, and P. Miles. 2015. MULTIPULSE – high resolution and high power in one TDEM system. *Exploration Geophysics* **46(1)**: 49-57, DOI: 10.1071/EG14027

Davis, A.C., J. Macnae, and T. Robb. 2006. Pendulum motion in airborne HEM systems. *Exploration Geophysics* **37(4)**: 355-362, DOI: 10.1071/EG06355

Davis, A., J. Macnae, and G. Hodges. 2009. Predictions of bird swing from GPS coordinates. *Geophysics* **74(6)**: F119–F126. DOI: 10.1190/1.3237143

Desmarais, J.K. 2018a. On closed-form expressions for the approximate electromagnetic response of a sphere interacting with a thin-sheet — Part 1: Theory in the frequency and time domain. *Geophysics* **84(3)**: E199–E198. doi: 10.1190/geo2017-0498.1.

Desmarais, J.K. 2018b. On closed-form expressions for the approximate electromagnetic response of a sphere interacting with a thin sheet — Part 2: Theory in the moment domain, validation, and examples. *Geophysics* **84(3)**: E189–E207, doi: 10.1190/geo2019-0128.1

Fugro (Fugro Airborne Surveys). 2005a. *Logistics and processing report, airborne magnetic and GEOTEM® survey, Russell South & Russell West, Saskatchewan, Job No. 05407*. Report for Roughrider Uranium Corp.

Fugro (Fugro Airborne Surveys). 2005b. *Basic EM interpretation report, airborne magnetic and GEOTEM® survey, Russell South & Russell West, Saskatchewan, Job No. 05407*. Report for Roughrider Uranium Corp.

Farquharson, C.G., D.W. Oldenburg and P.S. Routh. 2003. Simultaneous 1D inversion of loop-loop electromagnetic data for magnetic susceptibility and electrical conductivity. *Geophysics* **68**: 1857-1869.
<https://doi.org/10.1190/1.1635038>

Fullagar, P.K., and R. Schaa. 2014. Fast 3D inversion of transient electromagnetic (TEM) resistive limit data. *SEG Technical Program Expanded Abstracts 2014*: 1827-1831. <https://doi.org/10.1190/segam2014-1157.1>

Fullagar, P.K., G.A. Pears, J.E. Reid, and R. Schaa. 2015. Rapid approximate inversion of airborne TEM. *Exploration Geophysics* **46**: 112-117. <https://doi.org/10.1071/EG14046>

Hall, D. 2014. Classification of cued metalmapper data using data mining techniques. *Symposium on the Application of Geophysics to Engineering and Environmental Problems 2014*: 443-451.

<https://doi.org/10.4133/SAGEEP.27-150>

Hyde, C. 2002. The electromagnetic response of a sphere in the moment domain: A building block for the construction of arbitrary 3D shapes. *SEG Technical Program Expanded Abstracts 2002*: 645-648.

<https://doi.org/10.1190/1.1817335>

Jupp, D.L.B. and K. Vozoff. 1975. Stable iterative method for the inversion of geophysical data. *Geophysical Journal International* **42**: 957-976. <https://doi.org/10.1111/j.1365-246X.1975.tb06461.x>

Lane, R., A. Green, C. Golding, M. Owers, P. Pik, C. Plunkett, D. Sattel, and B. Thorn. 2000. An example of 3D conductivity mapping using the TEMPEST airborne electromagnetic system. *Exploration Geophysics* **31 (1-2)**: 162-172, DOI: 10.1071/EG00162

Lee., T.J., and R. Ignetik. 1994. Transient electromagnetic response of a halfspace with exponential conductivity profile and its applications to salinity mapping. *Exploration Geophysics* **25**: 39-51.
<https://doi.org/10.1071/EG994039>

Lee, T.J., and R.S. Smith. 2021. Multiple-order moments of the transient electromagnetic response of a one-dimensional earth with finite conductance – theory. *Exploration Geophysics* **52**: 1-15.
<https://doi.org/10.1080/08123985.2020.1760715>

Lee, T.J., R.S. Smith and C.S.B. Hyde. 2003. A non-integer moment of the impulse response for a conductive halfspace. *Geophysical Prospecting* **51**: 443-446. <https://doi.org/10.1046/j.1365-2478.2003.00383.x>

Morrison, H.F., R.J. Phillips, and D.P. O'Brien. 1969. Quantitative interpretation of transient electromagnetic fields over a layered half space. *Geophysical Prospecting* **17**: 82 – 101 DOI:
<https://doi.org/10.1111/j.1365-2478.1969.tb02073.x>

Press, W.H., S.A. Teukolsky, W.T. Vetterling, and B.P. Flannery. 1992. *Numerical Recipes in Fortran 77; The Art of Scientific Computing (Second Edition)*. Cambridge University Press.

Schaa, R., and P.K. Fullagar. 2010. Rapid, approximate 3D inversion of transient electromagnetic (TEM) data. *SEG Technical Program Expanded Abstracts 2010*: 650-654. <https://doi.org/10.1190/1.3513866>

Schaa, R. and P.K. Fullagar. 2012. Vertical and horizontal resistive limit formulas for a rectangular-loop source on a conductive half-space. *Geophysics* **77 (1)**: E91-E99. <https://doi.org/10.1190/geo2011-0141.1>

Smith, R.S. 2000. The realizable resistive limit: A new concept for mapping geological features spanning a broad range of conductivities. *Geophysics* **65**: 1124-1127. <https://doi.org/10.1190/1.1444805>

Smith, R.S. and A.P. Annan. 2000. Using an induction coil sensor to indirectly measure the B-field response in the bandwidth of the transient electromagnetic method. *Geophysics* **65**: 1489-1494.
<https://doi.org/10.1190/1.1444837>

Smith, R.S., and M.C. Chouteau. 2006. Combining airborne electromagnetic data from alternating flight directions to improve data interpretability: the virtual symmetric array. *Geophysics* **71**: G35-G41. doi: 10.1190/1.2187745

Smith, R.S., and T.J. Lee. 2001. The impulse-response moments of a sphere in a uniform field, a versatile and efficient electromagnetic model. *Exploration Geophysics* **32**: 113-118.

<https://doi.org/10.1071/EG01113>

Smith, R.S., and T.J. Lee. 2002a. The moments of the impulse response: a new paradigm for the interpretation of electromagnetic data. *Geophysics* **67**: 1095-1103. <https://doi.org/10.1190/1.1500370>

Smith, R.S., and T.J. Lee. 2002b. Using the moments of a thick layer to map the conductance and conductivity from airborne electromagnetic data. *Journal of Applied Geophysics* **49**: 173-183.

[https://doi.org/10.1016/S0926-9851\(01\)00112-4](https://doi.org/10.1016/S0926-9851(01)00112-4)

Smith, R.S., and T.J. Lee. 2003. Errata To "The moments of the impulse response: A new paradigm for the interpretation of transient electromagnetic data" (Richard S. Smith and Terry J. Lee, Geophysics 67: 1095-1103). *Geophysics* **68 (1)**: 409 -409. <https://doi.org/10.1190/1.1553688>.

Smith, R.S. and A.S. Salem. 2007. A discrete conductor transformation of airborne electromagnetic data. *Near Surface Geophysics* **5**: 87-95. <https://doi.org/10.3997/1873-0604.2006021>

Smith, R.S., C. Hyde, T. Lee, and R. Almond. 2003. Impulsive moments at work: *Proceedings of the 3DEM-3 symposium*, Australian Society of Exploration Geophysicists.

Smith, R.S., T.J. Lee, A.P. Annan, and M.D. O'Connell, 2005. Approximate apparent conductance (or conductivity) from the realizable moments of the impulse response. *Geophysics* **70 (1)**: G29-G32.

<https://doi.org/10.1190/1.1852776>

Smith, R.S., M.D. O'Connell, and L.H. Poulsen, 2004, Using airborne electromagnetic surveys to map the hydrogeology of an area near Nyborg, Denmark. *Near Surface Geophysics* **2**: 123-130.

<https://doi.org/10.3997/1873-0604.2004009>

Snyder, D.D., M. Prouty, D.C. George, T. King, M. Poulton, and A. Szidarovszky. 2010. UXO Discrimination at Camp San Luis Obispo with the MetalMapper. *Symposium on the Application of Geophysics to Engineering and Environmental Problems* 2010: 1054-1064. <https://doi.org/10.4133/1.3445421>

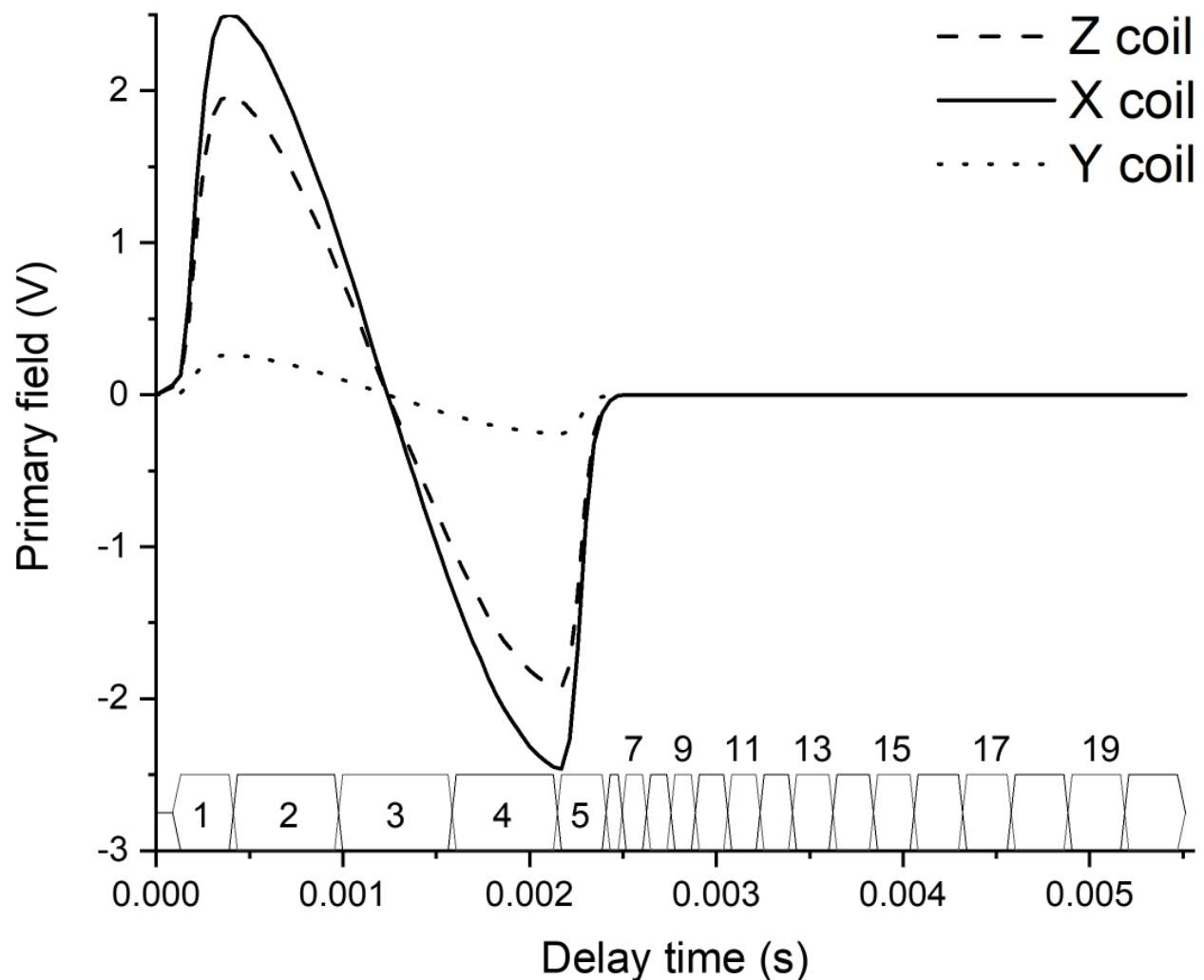
FIGURE CAPTIONS

Figure 1. The primary-field dB/dt voltage waveforms as measured at the receiver by the x -, y - and z -component sensor coils. The pulse is 2.2 ms in width and half the base period (the length of the pulse and the off time) is 5.555 ms (90 Hz base frequency). The positions of all the on-time window positions (1 to 5) are shown and labelled. The off-time window positons are also shown (windows 6 to 20), but due to space constraints, only the odd windows are labelled.

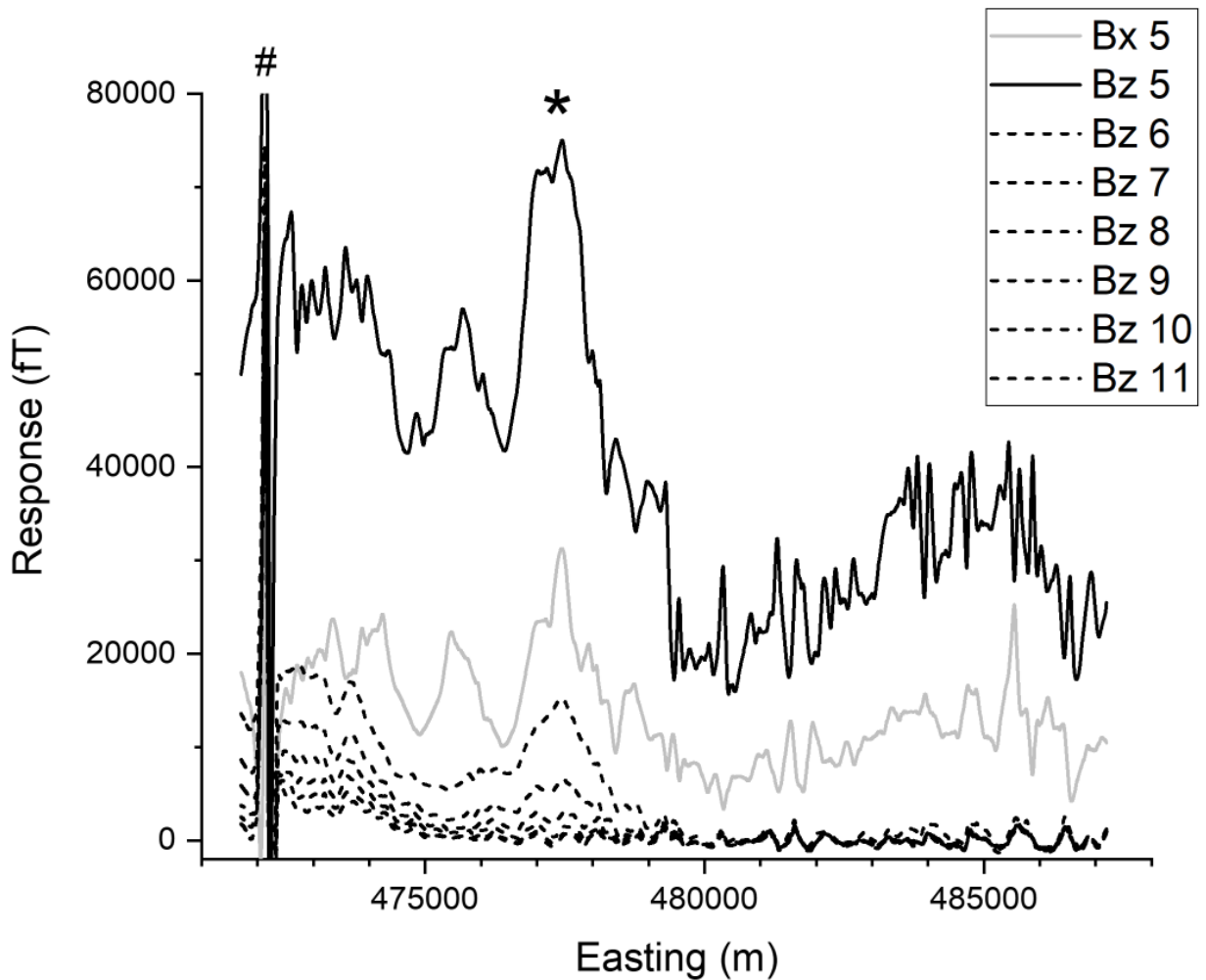


Figure 2. Electromagnetic response profile along line 143. The on-time z - and x -component responses are shown with the black and grey solid lines and the first six off-time windows (6 to 11) of the z -component are shown with the dashed lines. The asterisk symbol (*) denotes a weakly conductive location and the number symbol (#) shows where the profile crosses a power line. The map view on Figure 4c shows the location of line 143 (black arrows), the weakly conductive location (marked with an asterisk) and the power-line path (white line).

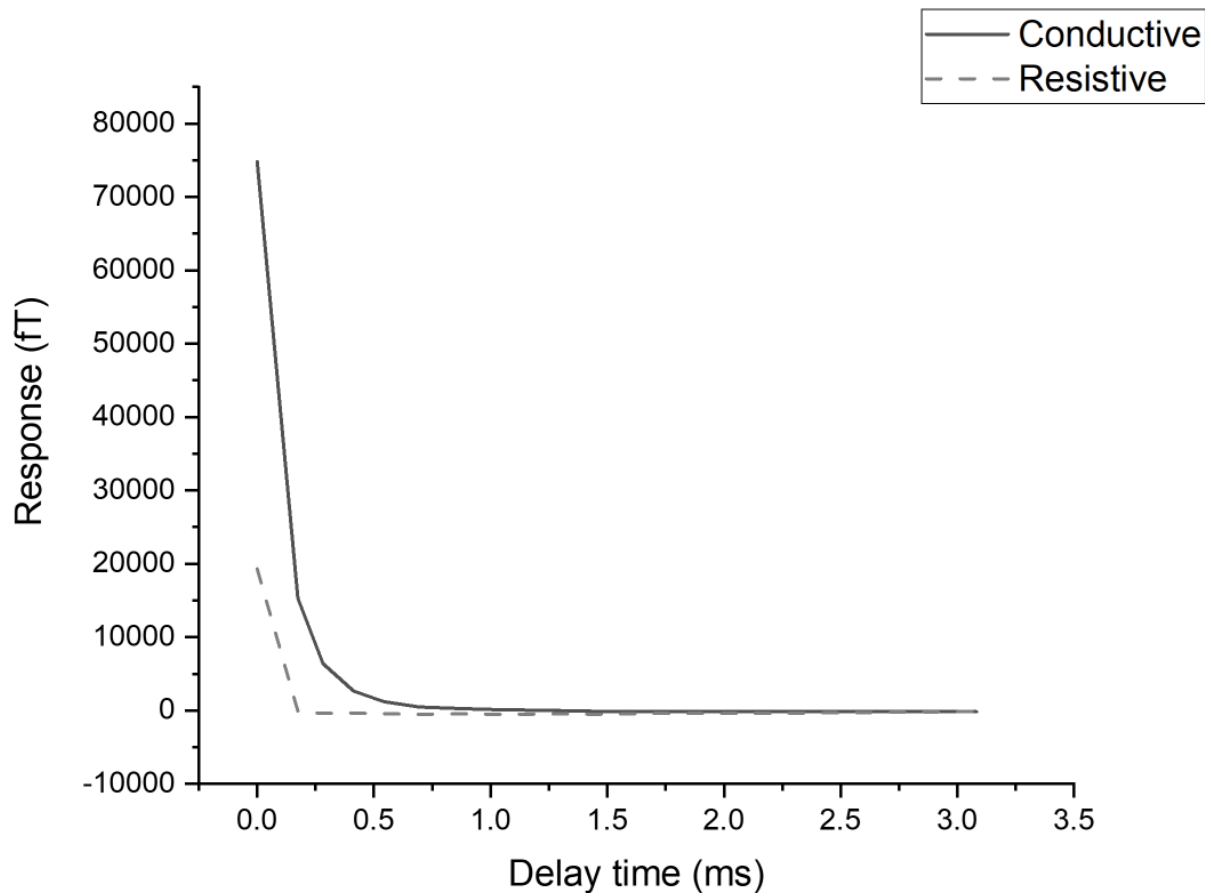


Figure 3. Some typical decays from line 143 at i) a weakly conductive location (near 477500 E, marked with an asterisk on Figure 2), shown with the solid line and ii) a location typical of much more resistive ground near 480000 E, where the response is effectively zero, except in the on-time (dashed line).

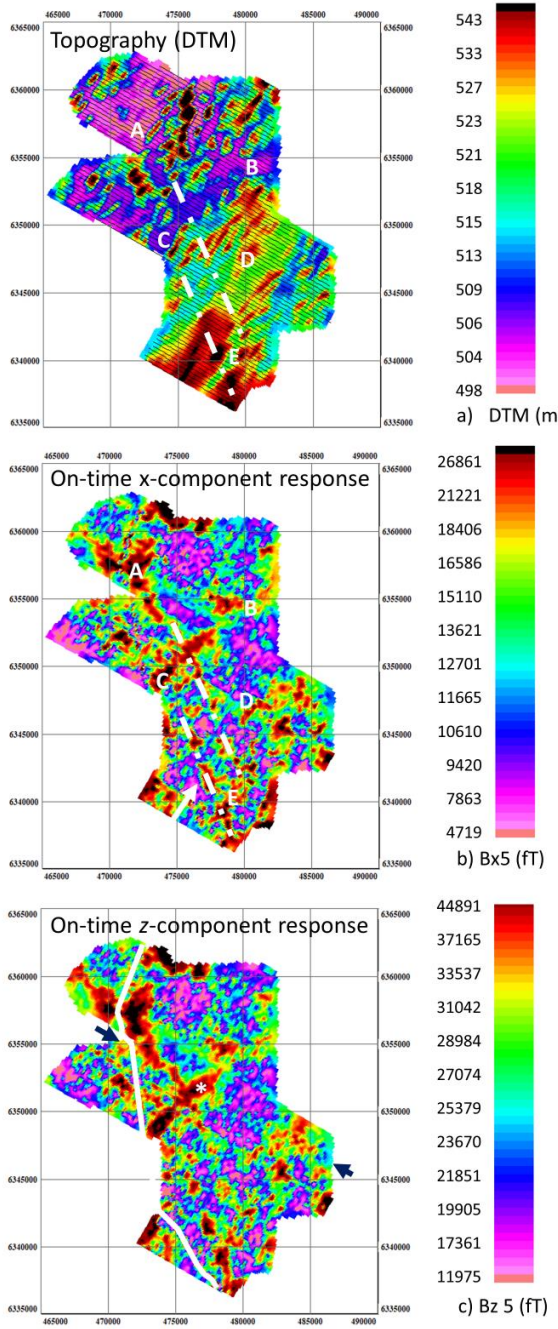


Figure 4. a) The digital terrain model (DTM) or height of the terrain above the WGS84 datum. b) The window 5 x-component response over the survey area. c) The window 5 z-component response over the survey area. The location of the anomaly marked * in Figure 2, the path of the power line (white line) and the location of line 143 (between the black arrows) are all shown on Figure 4c. The distance between grid lines in the map is 5 km. For colour images, see the on-line version of the paper.

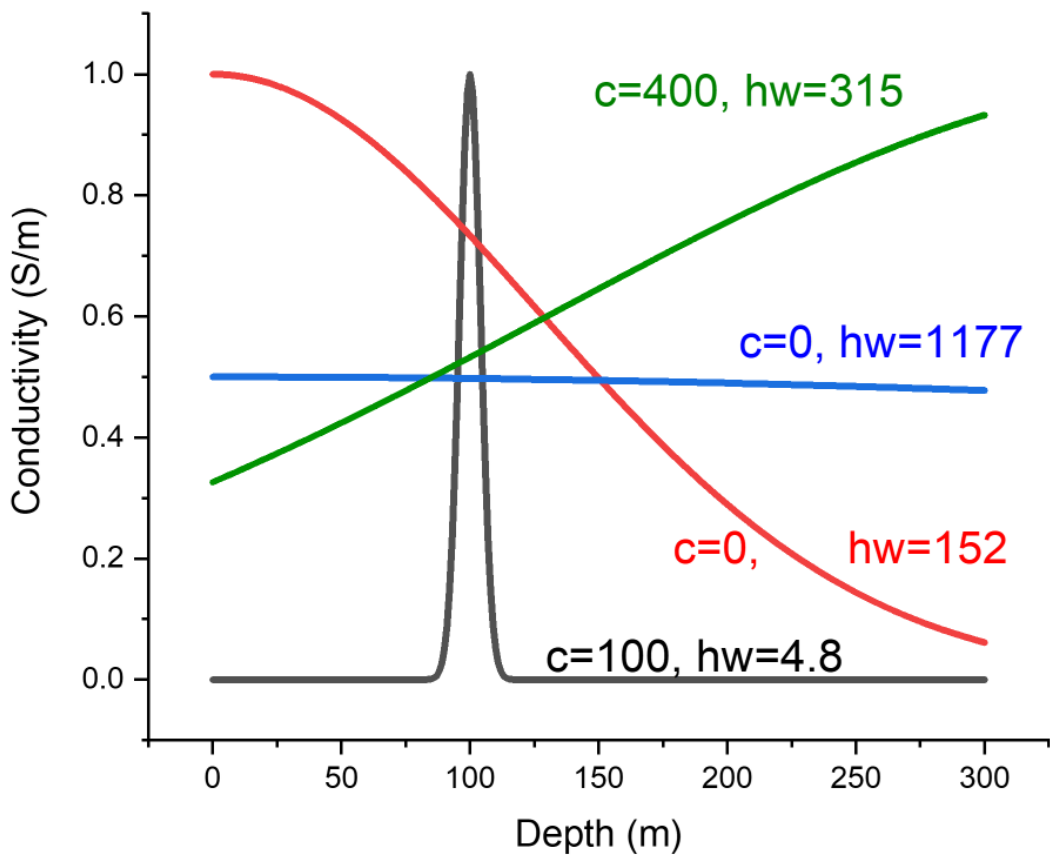


Figure 5. Conductivity variations with depth for a variety of combinations of parameters of the Gaussian model. The black curve is representative of a thin sheet at 100 m depth; the red curve is representative of a thick sheet with a half width of 150 m; the blue curve is representative of a half space; and the green curve a conductivity structure which increases gradually with depth. In all cases $A_0 = 1$, except the blue case, which is half this value.

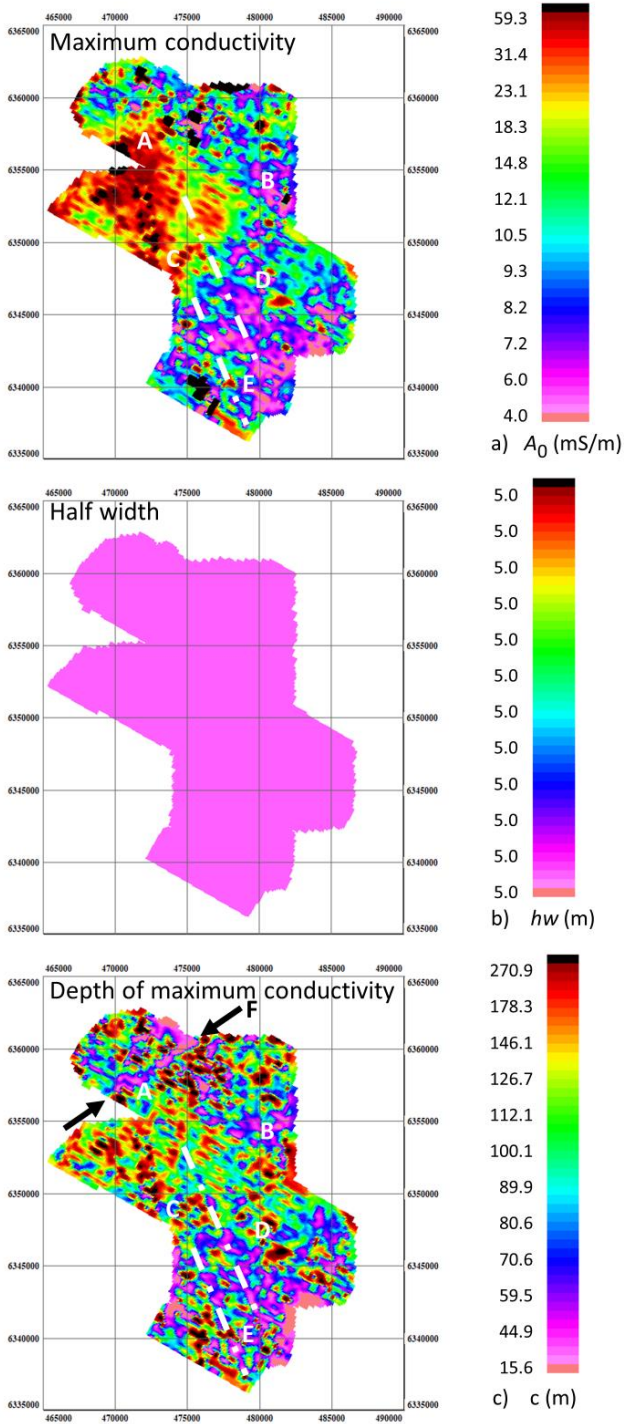


Figure 6. The maximum conductivity, A_0 , the half width, hw and depth of maximum conductivity, c for the case when the half width is constrained to be thin, $hw = 5$ m. The black arrow at the top pf panel c highlights a shallow linear feature, F, not evident on previous images. The labelled features are discussed in the text.

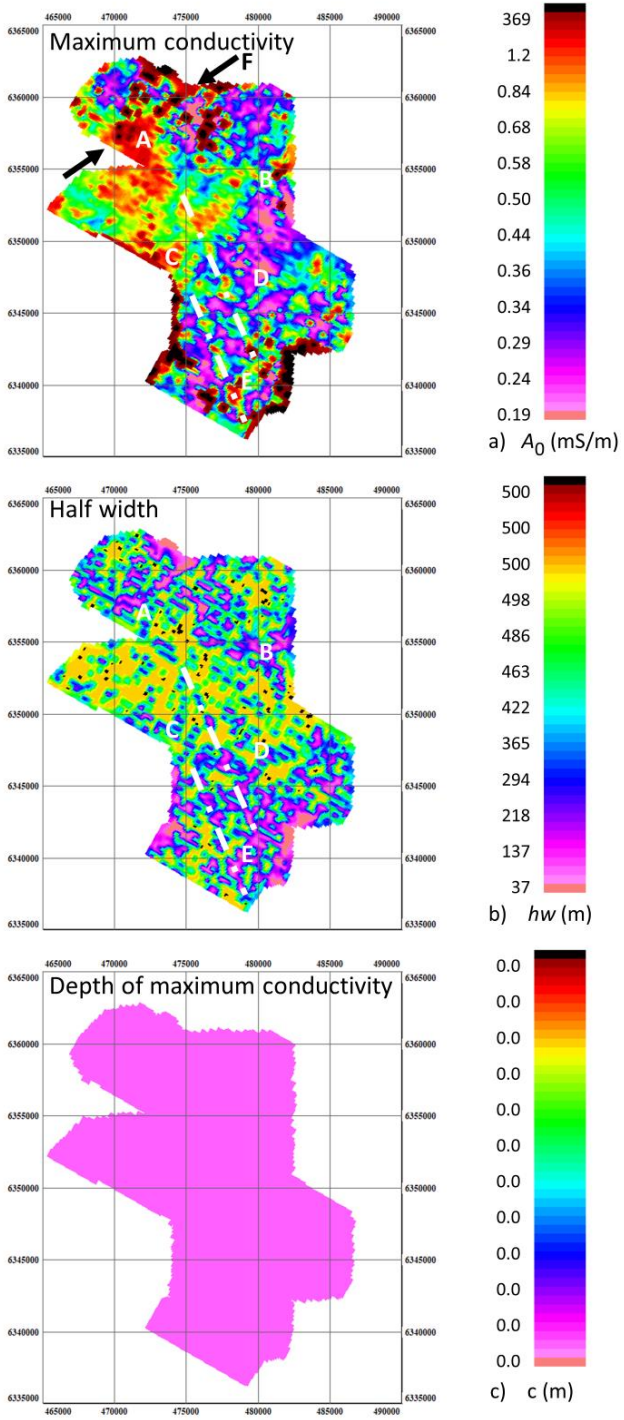


Figure 7. The maximum conductivity, A_0 , the half width, hw and depth of maximum conductivity, c for the case when the depth of the conductivity maximum is constrained to be at $c = 0$ m. Feature F is apparent on the maximum conductivity image, panel a) and as a feature with a small half width on panel b). The colour scales are different from those used in the previous figure.

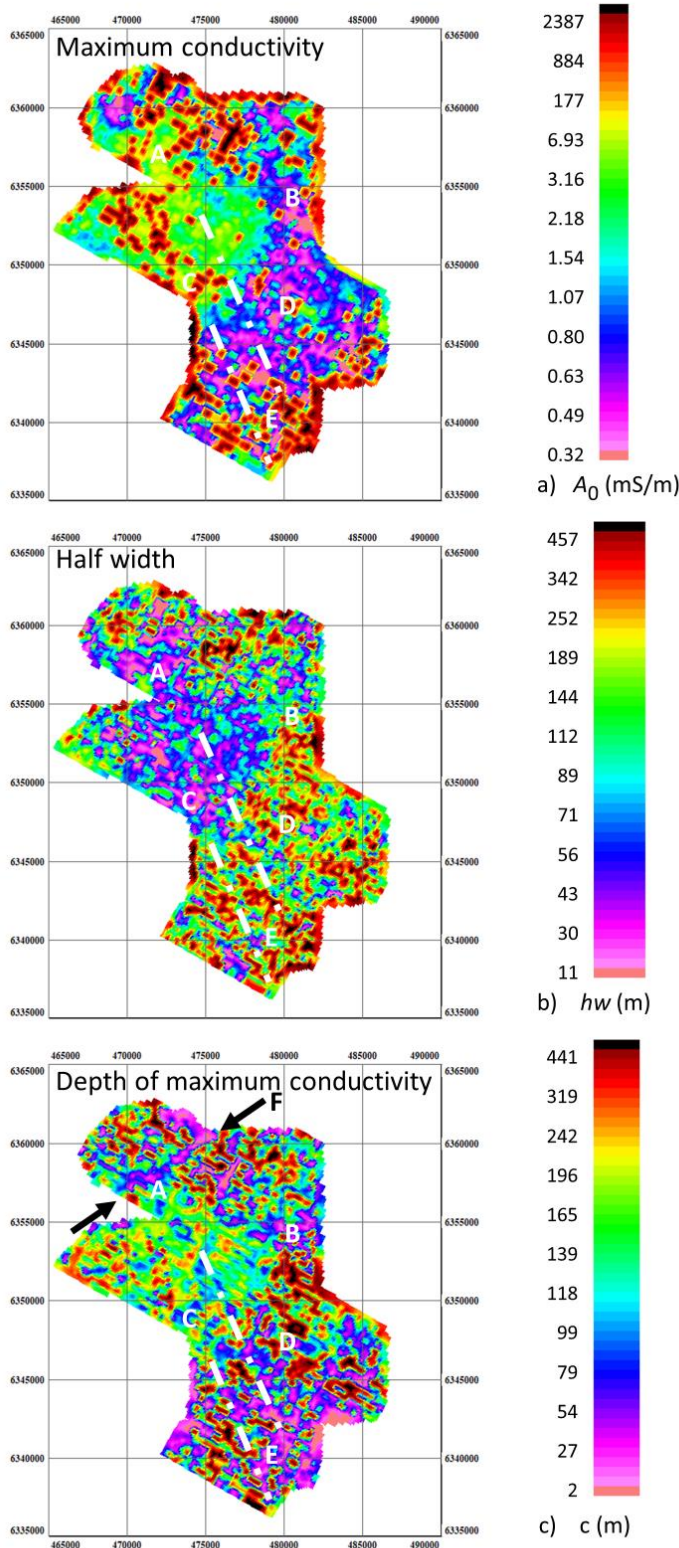


Figure 8. The maximum conductivity, A_0 , the half width, hw and depth of maximum conductivity, c when there are no constraints. The colour scales are different from those used in the previous figures.

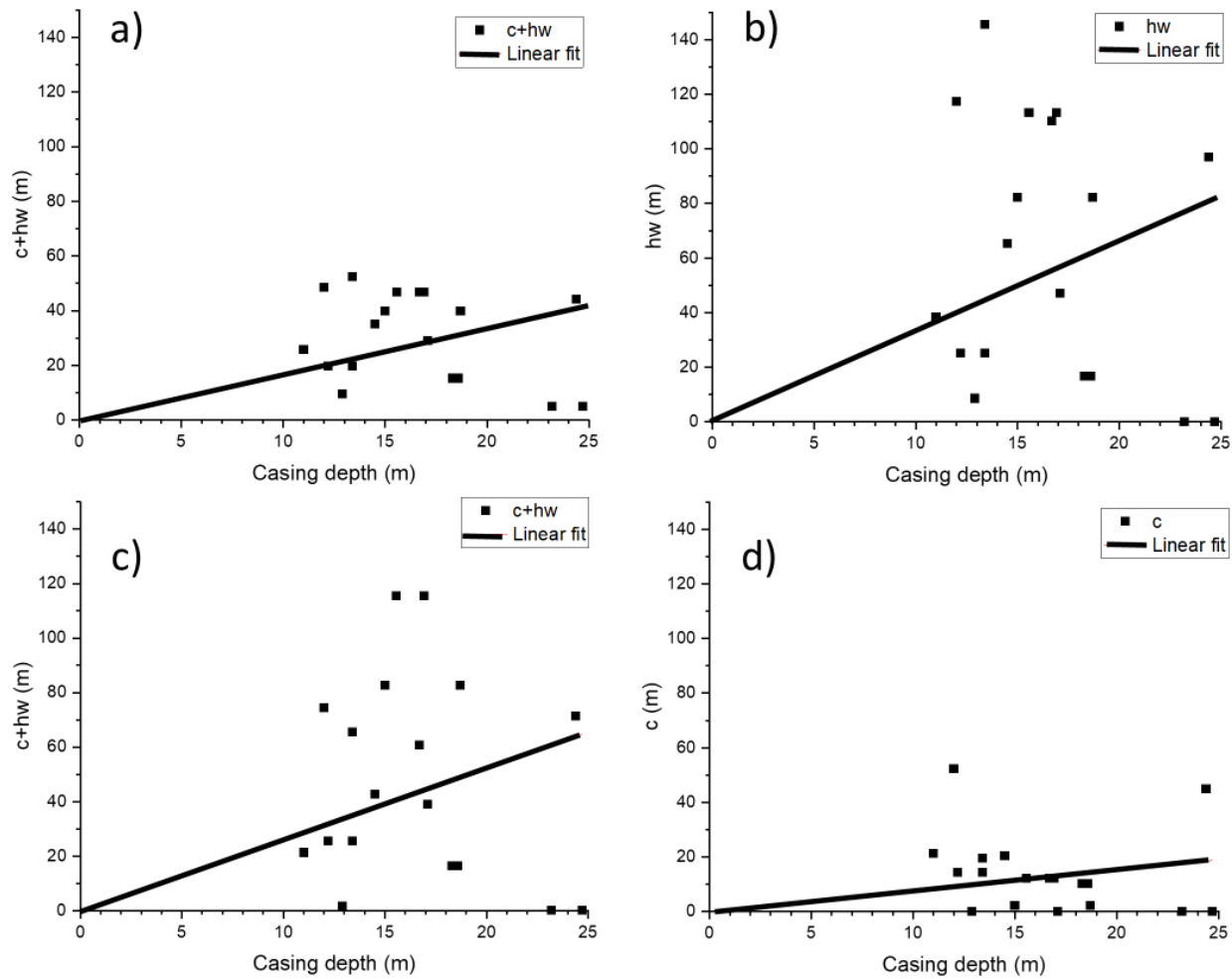


Figure 9. Cross plots of the depth parameters derived from different inversions compared with the drill-hole casing depth, considered as an overestimate of the overburden thickness. a) The case when the base of the Gaussian model is constrained to be a thin sheet with $hw = 5.0$. b) The case when the base of the Gaussian model is constrained to be a thick sheet at surface ($c = 0$). c) The base of an unconstrained Gaussian model ($c + hw$). d) The depth of maximum conductivity, c , of the same unconstrained Gaussian model.

TABLE CAPTION AND TABLE

Table 1. Parameters quantifying linear fits to cross plots of the estimated depth as a function of the casing depth. In all cases the intercept is constrained to be at the origin.

	Slope	Residual sum of squares	Pearson's r	R-Square (COD)
Case 1: $hw = 5.0$ Fit to $c + hw$	1.65 ± 0.26	6401	0.836	0.699
Case 2: $c = 0$ Fit to hw	3.30 ± 0.69	47147	0.745	0.555
Case 3: unconstrained Fit to $hw + c$	2.62 ± 0.54	28053	0.755	0.570
Case 3: unconstrained Fit to c	0.76 ± 0.21	4142	0.655	0.429